Applied Physics Letters

Strain control of phase transition and magnetocaloric effect in $Nd_{0.5}Sr_{0.5}MnO_3$ thin films

Cite as: Appl. Phys. Lett. **116**, 082402 (2020); https://doi.org/10.1063/1.5134116
Submitted: 30 October 2019 . Accepted: 15 February 2020 . Published Online: 25 February 2020

Yao Liu, Tianyu Ma, Kaiming Qiao, Jia Li, Andong Xiao, Jing Wang, Fengxia Hu, and Baogen Shen

Applied Physics Letters ARTICLE scitation.org/journal/apl

Strain control of phase transition and magnetocaloric effect in $Nd_{0.5}Sr_{0.5}MnO_3$ thin films

Cite as: Appl. Phys. Lett. **116**, 082402 (2020); doi: 10.1063/1.5134116
Submitted: 30 October 2019 · Accepted: 15 February 2020 ·
Published Online: 25 February 2020

Yao Liu,[1] Tianyu Ma,[1,a)] Kaiming Qiao,[2] Jia Li,[2] Andong Xiao,[1] Jing Wang,[2] Fengxia Hu,[2,3,a)] and Baogen Shen[2]

AFFILIATIONS

[1]Frontier Institute of Science and Technology, State Key Laboratory for Mechanical Behavior of Materials, and MOE Key Laboratory for Nonequilibrium Synthesis and Modulation of Condensed Matter, Xi'an Jiaotong University, Xi'an 710054, China
[2]Beijing National Laboratory for Condensed Matter Physics and State Key Laboratory of Magnetism, Institute of Physics, Chinese Academy of Sciences, Beijing 100190, China
[3]Songshan Lake Materials Laboratory, Dongguan, Guangdong 523808, China

[a)]**Authors to whom correspondence should be addressed:** matianyu@xjtu.edu.cn and fxhu@iphy.ac.cn

ABSTRACT

Phase transition and the magnetocaloric effect (MCE) in $Nd_{0.5}Sr_{0.5}MnO_3$ (NSMO) epitaxial thin films were tailored through controlling the lattice-mismatch-induced-strain by depositing on (011)—$(La_{0.18}Sr_{0.82})(Al_{0.59}Ta_{0.41})O_3$ and $SrTiO_3$ (STO) single crystalline substrates, respectively. The NSMO film grown on STO, exhibiting uniaxial like tensile strain of 1.3% along the in-plane [100] direction, undergoes a paramagnetic to ferromagnetic transition at ~210 K followed by a ferromagnetic to A-type antiferromagnetic transition at ~179 K upon cooling; meanwhile, the film grown on LSAT, exhibiting anisotropic in-plane tensile strains of 0.36% along [100] and 0.50% along $[0\bar{1}1]$ directions, undergoes further transition to CE-type antiferromagnetic transition at ~145 K. NSMO/LSAT with such transitions facilitates a strong MCE over a much wider temperature range from 90 to 170 K, with the magnetic entropy change comparable to the recently reported $La_{0.25}Ca_{0.75}MnO_3$ bulk. These findings suggest that control of strain in manganite films with first-order phase transition is a feasible way to broaden their MCE temperature range.

The magnetocaloric effect (MCE), which manifests itself as an adiabatic temperature change under the stimulation of magnetic field, has shown great potential in the refrigeration technique. The discovery of a giant MCE in materials with first-order phase transition, such as $Gd_5(Si,Ge)_4$, $La(Fe,Si)_{13}$, Fe–Rh, NiMn-based Heusler alloys, manganite systems *etc.*,[1–8] enables the possible applications of the magnetic refrigeration technique in the vicinity of room temperature. Due to the fact that first-order phase transition occurs at a certain temperature, the giant MCE can merely be obtained over a narrow temperature range that spreads this certain temperature.[5,6] Consequently, broadening the MCE temperature range in materials with first-order phase transition has stimulated extensive research over decades.

Several strategies have been proposed to broaden the MCE temperature range through manipulating the underlying phase transition behaviors.[9–15] Assembling multi-component MCE materials with various phase transition temperatures together has been proved to be effective in extending the MCE temperature range,[10–13] for example, six layers of $La(Fe,Si)_{13}H_y$ alloys with progressively varying composition enable a broader cooling temperature range of 14 K than that of the individual components, which have a cooling temperature range of only 2 K.[10] This strategy has also been found to be effective in $Gd_{1-x}Dy_x$,[11] $La_{2/3}(Ca_{1-x}Sr_x)_{1/3}MnO_3$[12] and $Tb_x(Dy_{0.5}Ho_{0.5})_{1-x}Co_2$ $(0 \leq x \leq 0.5)$[13] systems, which may promote their potential applications in refrigeration devices. However, the multi-component composites are difficult to manufacture and will introduce larger thermal resistance.[10,11] External fields can also be used to broaden the MCE temperature range by tailoring the phase transition of the materials.[14,15] By applying electric fields on the hybrid Ni–Co–Mn–In/PMN–PT composites, the stress induced in PMN–PT will exert on the Ni–Co–Mn–In alloy and tune the transformation temperature largely, which can facilitate a large MCE over a wide temperature range from 278 K to 293 K.[15] Unfortunately, the use of extra electric field makes the design of prototype more complicated. Consequently, it would be ideal to realize a large MCE over a wide temperature range in a single-component material without the need for extra external fields.

We notice that growing epitaxial films on single crystalline substrates can induce in-plane strains, which can tune the phase transition behaviors effectively.[16–19] For example, through depositing MnAs

films on GaAs substrates with different crystalline orientations of (001) and (111), compressive strains can be induced, which alters the first-order phase transition temperature and MCE accordingly.[16] Besides the first-order phase transition alloys, there is a large class of manganite that may serve as potential magnetic refrigerants for their significant MCE accompanying the diverse magnetic transitions.[20–25] If the phase transition behavior was tailored by introducing strain through depositing films, it would be promising to obtain a considerable MCE over a wide temperature range in the single film. In this Letter, this proposed strategy is applied on the $Nd_{1-x}Sr_xMnO_3$ systems. The first-order phase transition from high temperature ferromagnetic (FM) to low temperature charge ordering (CO) phase with a CE-type AFM magnetic configuration ($0.49 \leq x \leq 0.51$)[26] is accompanied by a MCE with a magnetic entropy change of 7 J/kgK.[21] In addition, the A-type AFM phase can also form between the FM and CE-type AFM phase.[26–28] In the following, we shall show that tailoring the FM to AFM phase transition by controlling the in-plane strains in $Nd_{0.5}Sr_{0.5}MnO_3$ (NSMO) epitaxial films on different substrates indeed facilitates a large MCE over a wide temperature range from 90 to 170 K.

NSMO films were epitaxially deposited using the pulsed laser deposition (PLD) technique with a 248 nm KrF excimer laser. The $Nd_{0.5}Sr_{0.5}MnO_3$ target was prepared by the solid-state reaction method.[28] The room temperature x-ray diffraction (XRD, see Fig. S1 in the supplementary material) results show that the target has an orthorhombic structure with lattice constants of $a = 5.473$ Å, $b = 5.426$ Å, and $\sqrt{2}c = 5.391$ Å ($a = b = 3.858$ Å, and $c = 3.812$ Å in the cubic notation).[26] Thin films were grown on (011)-oriented $SrTiO_3$ (STO, $a = 3.905$ Å) and $(La_{0.18}Sr_{0.82})(Al_{0.59}Ta_{0.41})O_3$ (LSAT, $a = 3.868$ Å) substrates, respectively. During deposition, the substrate temperature was kept at 700 °C and the O_2 pressure was maintained at 50 Pa, the laser energy density and frequency were fixed at 1.5 J/cm^2 and 2 Hz, respectively. After deposition, the films were subjected to *in situ* post-annealing for 0.5 h at 700 °C with an O_2 pressure of 100 Pa. The film thickness was carefully controlled by deposition time and determined to be 60 nm by the x-ray reflectometry (XRR, Fig. S2) technique. The specific thickness 60 nm was selected, because it has been revealed that the AFM phases would form within 50 nm–110 nm and the film properties show no essential dependence on the thickness within this range.[29] The film structure was identified by the XRD pattern and reciprocal space maps (RSMs) using a high-resolution Bruker D8 four circular x-ray diffractometer with Cu–Kα radiation. The interfacial microstructures were characterized using high-resolution transmission electron microscopy (HR-TEM). The temperature dependences of magnetization (M-T) and resistivity (ρ-T) were also measured to detect the associated phase transitions. M-T plots with zero field cooling (ZFC), field cooling (FC), and field heating (FH) modes were adopted with a 0.05 T magnetic field applied along the in-plane [100] direction of the substrate. ρ-T curves with both heating and cooling plots were recorded without magnetic field. After zero field cooled to 50 K, isothermal magnetization curves were recorded upon heating with a temperature interval of 10 K along the in-plane [100] direction of the substrate (Quantum Design SQUID-VSM system). X-ray absorption spectroscopy (XAS) measurements in total electron yield mode were carried out to check the variation in oxygen vacancies of the films at a Beamline BL08U1A of Shanghai Synchrotron Radiation Facility with an energy resolution of 0.3 eV.

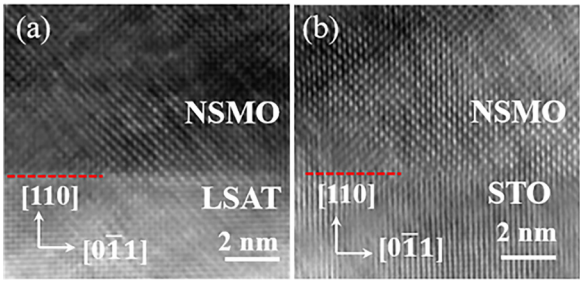

FIG. 1. High resolution TEM images for NSMO/LSAT (a) and NSMO/STO (b) films taken from the [100] zone axis of the substrates, where the red dashed lines indicate the interfaces.

Figure 1 shows the HR-TEM images of the cross sections for NSMO films grown on LSAT [Fig. 1(a)] and STO [Fig. 1(b)] substrates, respectively. The images were taken by tilting the substrates along their [100] zone axis. Both images reveal the epitaxial growth of NSMO films on the (011) planes of LSAT and STO. Due to the lattice mismatch between the coherent NSMO and the substrates, the strain state varies greatly between these two samples with fixed thickness, and the difference was determined by the room temperature XRD patterns and RSM shown in Fig. 2. From the XRD patterns [Figs. 2(a) and 2(d)], the average out-of-plane lattice spacing $d_{(011)}$ can be calculated to be 2.697 Å and 2.689 Å for NSMO/LSAT and NSMO/STO, both are smaller than that of the NSMO target (2.712 Å), indicating the tensile strain along in-plane directions.

The in-plane lattice strains along [100] and [0$\bar{1}$1] directions were identified from the (222) and (013) reflections in RSMs.[30,31] The strains are estimated using $(d_f\text{-}d_{bulk})/d_{bulk}$, where d_f and d_{bulk} are the lattice spacings of the films and bulk, respectively. In Figs. 2(b) and 2(c), one can see that the (222) and (013) reflections for the NSMO film have the same Q values with the LSAT substrate along [100] and [0$\bar{1}$1] directions, meaning that the film is constrained and has the same in-plane lattice spacings as those for the LSAT substrate, that is,

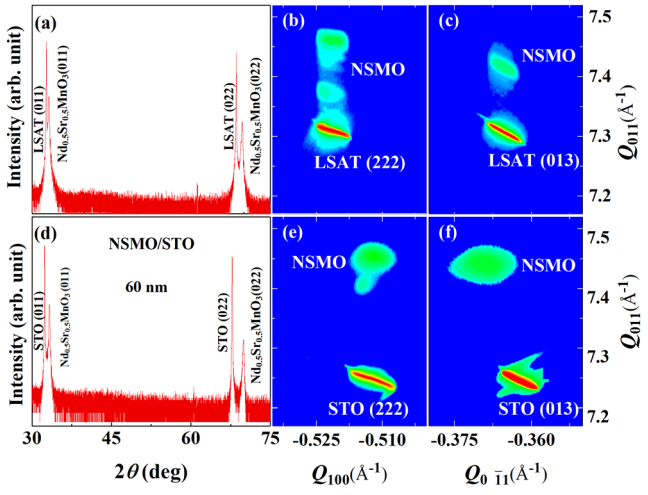

FIG. 2. XRD patterns and reciprocal space maps with both (222) and (013) reflections for NSMO/LSAT (a)–(c) and NSMO/STO (d)–(f).

$d_{f-[100]} \approx d_{LSAT-[100]} = 3.868$ Å and $d_{f-[0\bar{1}1]} \approx d_{LSAT-[0\bar{1}1]} = 2.761$ Å. The calculated tensile strains along in-plane [100] and [0$\bar{1}$1] directions are 0.36% and 0.50%, respectively. In contrast, though the (222) reflection for the NSMO film has the same Q value as the STO substrate along the [100] axis [Fig. 2(e)], the (013) reflection for the NSMO film has a distinct Q value with the STO substrate along the [0$\bar{1}$1] axis [Fig. 2(f)]. It indicates that the lattice spacing $d_{f-[100]}$ is elongated to fit that for STO with $d_{STO-[100]} = 3.905$ Å, resulting in an average tensile strain of 1.3% along the [100] axis. From the $|Q|$ value, the $d_{f-[0\bar{1}1]}$ can be calculated to be 2.713 Å, which is close to the $d_{[0\bar{1}1]}$ of bulk NSMO, meaning that NSMO on STO is almost relaxed along this direction. The comparative results reveal that NSMO films suffer from in-plane tensile strains along both [100] and [0$\bar{1}$1] directions when growing on the LSAT substrate, but suffer from uniaxial-like tensile strain along only the [100] direction when growing on the STO substrate.

The different in-plane strain states result in distinct phase transition behaviors and MCE between NSMO/LSAT and NSMO/STO. Figure 3 shows the temperature dependent magnetization and resistivity, respectively. Both samples undergo a transition from paramagnetic (PM) to FM state at ~210 K (T_C), as reflected by the M-T curves in Figs. 3(a) and 3(b). Upon further cooling, both samples exhibit apparent magnetization reduction, implying the transition from FM to AFM state. The hysteresis between heating and cooling processes reveals the first-order nature of this transition. The transition temperature is higher for NSMO/LSAT (190 K, cooling) than that for NSMO/STO (179 K, cooling), indicating that this first-order phase transition temperature can be tailored through controlling the strains in the films. Below 145 K, the NSMO/LSAT sample exhibits an additional phase transition, manifested by the further magnetization reduction with thermal hysteresis Fig. 3(a). The ρ value of films gradually drops below the Curie temperature of 210 K for both films as shown in Figs. 3(c) and 3(d). Accompanying the subsequent FM to AFM transition at 190 K for NSMO/LSAT and 179 K for NSMO/STO, the ρ value denotes slight enhancement, indicating that this transition is from the FM into A-type AFM phase (T_N^A) with OO of [$d(x^2$-$y^2)$],[26,28] because

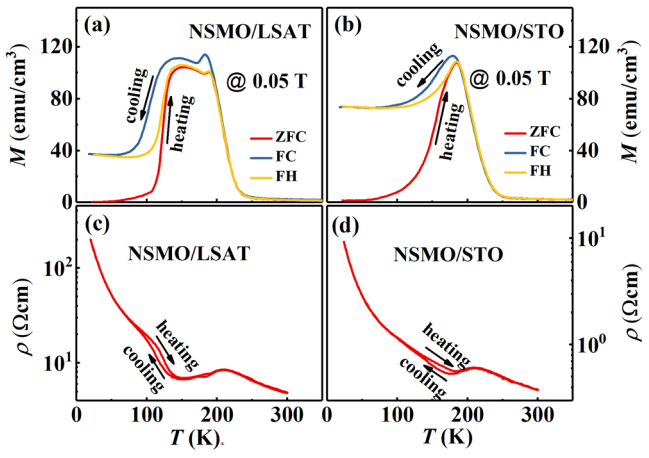

FIG. 3. Magnetization vs temperature curves with zero field cooling, field cooling, and field heating modes for NSMO/LSAT (a) and NSMO/STO (b) measured in a magnetic field of 0.05 T. Resistivity vs temperature curves for NSMO/LSAT (c) and NSMO/STO (d), where the arrows indicate the heating and cooling processes.

the A-type AFM phase is metallic within the OO (a-b) plane. Comparatively, below 190 K, the resistivity of NSMO/LSAT shows another sharp increase with thermal hysteresis below 145 K and subsequently enhances continuously with decreasing temperature, indicating a further phase transition. NSMO/STO, on the other hand, shows a monotonous increase in resistivity with decreasing temperature below 179 K without sign of another transition. The ρ value is nearly one order higher for NSMO/LSAT than that for NSMO/STO in the lower temperature of 20 K, suggesting that NSMO/LSAT experiences a further transition to insulating CE-type AFM (T_N^{CE}) phase.[26–28] The bare STO and LSAT substrates have cubic—tetragonal phase transitions at 105 K and 150 K, respectively.[32,33] This structural transition has been reported to be able to cause anomaly in magnetic and electronic properties of films on it.[34] However, as can be seen in M – T and ρ – T curves, no anomaly in magnetization and resistivity shows up in the NSMO/STO across 105 K and in the NSMO/LSAT across 150 K. This could be due to the fact that the strain effect exerted by the cubic—tetragonal phase is rather small in the (011)-oriented STO and LSAT substrates, the lattice spacing $d_{(011)}$ of both NSMO and STO changes continuously across the transition (Fig. S3). Besides, both STO and LSAT are diamagnetic and the magnetic susceptibility is nearly independent of the temperature (see Fig. S4); their contribution to the net magnetic transitions can thus be neglected.

The common FM to A-type AFM transition followed by further transition to CE-type AFM transition yields a considerate MCE over a much wider temperature range in NSMO/LSAT than that in NSMO/STO. As shown in Fig. 4, NSMO/LSAT exhibits two kinds of metamagnetic transitions over a wide temperature from 50 to 180 K, as reflected by the S shaped isothermal magnetization curves (with hysteresis between magnetization and demagnetization process) in Figs. 4(a) and 4(c). In contrast, the NSMO/STO film only exhibits obvious S shaped magnetization curves over a relatively narrower temperature range from 110 K to 170 K. Due to the analyzed phase transition process above, the S shaped magnetization curves within the temperature

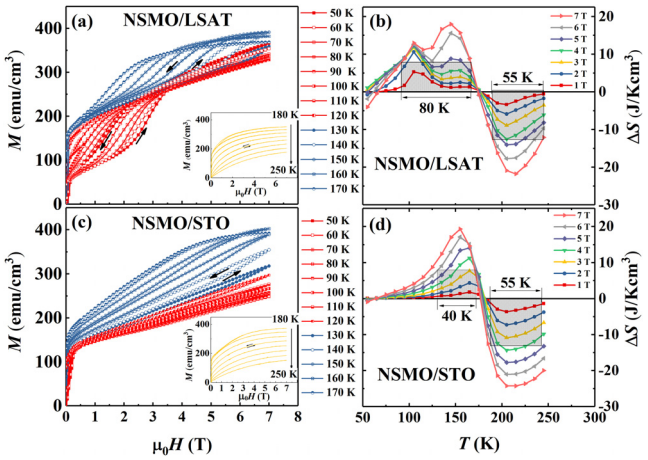

FIG. 4. Isothermal magnetization curves for NSMO/LSAT (a) and NSMO/STO (c), both insets give the M-H curves within the temperature range of 180 K–250 K, which corresponds to the second-order phase transition. Magnetic entropy change dependence on temperature for NSMO/LSAT (b) and NSMO/STO (d), where the shadow areas indicate the working temperature range.

range from 110 K to 180 K/170 K are due to the magnetic-field induced transition from A-type AFM to FM in both samples. The metamagnetic transition merely observed in NSMO/LSAT over the temperature range from 50 to 120 K should be due to the magnetic-field induced transition from the CE-type AFM to FM phase. For NSMO/STO within this temperature range, the rapid increase at the initial magnetization curves indicates the existence of FM phase. The direct connection of these two temperature ranges with metamagnetic transitions facilitates a considerate MCE over a wide temperature range in NSMO/LSAT. The magnetic entropy change (ΔS_M) calculated using the Maxwell relation from the isothermal magnetization curves is shown in Figs. 4(b) and 4(d). The effective cooling temperature range, which is identified as the temperature range corresponding to the half maximum of ΔS_M,[35] is indicated by the range within the shadow area here. It clearly reveals that NSMO/LSAT has a broader effective cooling temperature range of 80 K (from 90 K to 170 K) in a magnetic field change of 0–6 T, twice that for NSMO/STO (40 K, from 130 to 170 K). The ΔS_M induced by the metamagnetic transition is positive, implying the inverse MCE accompanying the first-order phase transition. The maximum ΔS_M values are 17.5 J/Kcm^3 at 160 K and 15.7 J/Kcm^3 at 120 K for NSMO/LSAT, while 18.6 J/Kcm^3 at 155 K for NSMO/STO, these values are comparable to those obtained in bulk $La_{0.25}Ca_{0.75}MnO_3$ and $La_{5/8-y}Pr_yCa_{3/8}MnO_3$ materials.[24,25] Besides, the largest conventional magnetic entropy change ΔS_M reaches −25 J/Kcm^3 around the Curie transition of 225 K for both samples.

As observed in the proof-of-principle reference, NSMO, a considerate MCE over a wide temperature range can be achieved by controlling the lattice strain of the epitaxial film. The lattice strain can play the role of connecting the effective cooling temperature ranges arisen from two metamagnetic transitions. NSMO has a strong interplay between charge, spin, orbital, and lattice ordering parameters.[26] The transformations from the orbital disordered FM state to orbital ordered A-type AFM and CO/CE-type AFM states are associated with lattice distortion. The *c* axis contracts by 1.5% and is the main deformation axis.[25,27] As a result, the transition from FM to both the A-type and CE-type phases can be tailored by the lattice strain.[30,31,36] It has been reported in NSMO bulk that applying uniaxial compressive stress along the *c* axis will raise the transition temperature from FM to both A-type and CE-type AFM phases.[36] Furthermore, as the CE-type AFM phase is coupled with CO, i.e., the Mn^{3+}/Mn^{4+} ions are alternatively aligned, the transition to the CE-type AFM will also be influenced by tuning the CO. In the present NMSO films, the *a* axis is constrained by the substrate, while the *b* and *c* axes lie out of plane. It means that the deformations along *b* or *c* axes are allowed during the cooling process, which, as has been reported,[29,30] facilitating the transition to the AFM phases in the NSMO films. Still, NSMO/STO experiencing a larger strain of 1.3% along the *a* axis enables only the FM to A-type AFM transition, and this transition is incomplete with remanence of the FM phase in the lower temperature. In contrast, the NSMO on LSAT which goes through small strains of 0.36% along the *a* axis and 0.50% along the $[0\bar{1}1]$ axis undergoes a further transition to the CE-type AFM phase transition after the partial transition from the FM to the A-type AFM state.

The suppression of transition to CO/CE-type AFM in NSMO/STO could be ascribed to a high strain state which prohibits the formation of the CO upon cooling. In $Nd_{1-x}Sr_xMnO_3$, CO is intimately related to the composition and happens only when Mn^{3+} and Mn^{4+} ions have a ratio of 1:1.[26] Consequently, the variation in concentration of oxygen vacancies will disturb the ratio between Mn^{3+} and Mn^{4+} ions and inhibit CO. As the concentration of oxygen vacancies in manganite films is known to be closely related to the strain,[37] we thus estimate the oxygen vacancy concentration of the present films by XAS. Figure 5 displays the oxygen (O) *K*-edge XAS spectra for both films. The relevant peak of the energy shoulder at 532.5 eV (pointed by the arrow) is due to dipole transitions from O 1*s* to O 2*p* states, and is hybridized with the unoccupied Mn 3*d* orbitals. The intensity of this peak can thus represent the oxygen vacancies.[38] The NSMO/STO film exhibits higher intensity at 532.5 eV, indicating that it contains more oxygen vacancies than that in NSMO/LSAT. In combination with the strain identification, it can be deduced that larger average strain in NSMO/STO will cause more oxygen vacancies, which certainly prohibits transition into the CO/CE-type AFM phase.

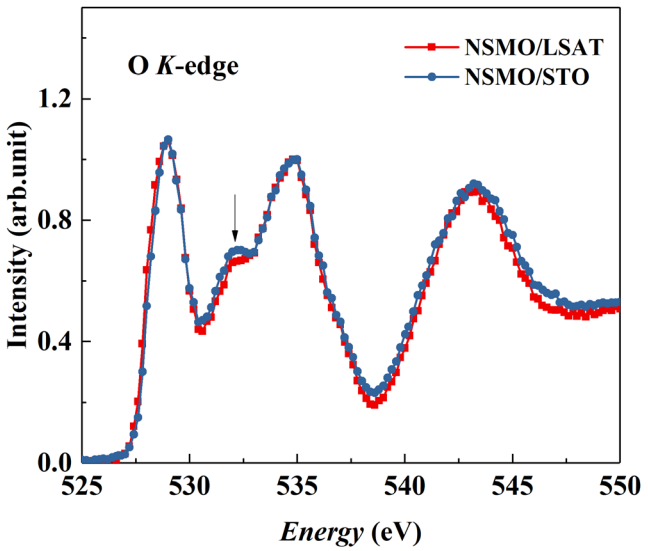

FIG. 5. Oxygen *K*-edge XAS spectra for NSMO/LSAT and NSMO/STO.

In summary, the present study demonstrates that introducing appropriate anisotropic strain to realize the successive first-order transitions from FM to A-type AFM and further to CO/CE-type AFM phase can broaden the MCE temperature range in NSMO films. Combining the conventional MCE around the Curie temperature, the NSMO/LSAT film exhibits possibilities of magnetic cooling within the temperature range of 90 K–245 K. Besides, the present study also suggests a further interesting route for NSMO based MCE applications in the micro-cooling devices, which is promising due to the increasing demand for the micro-electronic devices and their heat dissipation problem. Furthermore, this method can be applied in other manganite systems, which have diverse magnetic phase transitions with transition temperature close to room temperature.

See the supplementary material for the detailed information about the determination of the film thickness, the fabrication process and structure of the $Nd_{0.5}Sr_{0.5}MnO_3$ target, the structural evolution with temperature for NSMO/STO, and the magnetic properties of the bare substrates.

The authors acknowledge Beamline BL08U1A in Shanghai Synchrotron Radiation Facility (SSRF) for XAS measurements. This work was supported by the National Natural Sciences Foundation of China (Grant Nos. 51622104, 51871174, 51901170, 51531008, U1832219, and 51771223), the National Key Research and Development Program of China (Grant Nos. 2017YFB0702702 and 2017YFA0303601), and the Key Program and Strategic Priority Research Program (B) of the Chinese Academy of Sciences.

REFERENCES

[1]V. K. Pecharsky and K. A. Gschneidner, Jr., Phys. Rev. Lett. **78**, 4494 (1997).
[2]F. X. Hu, B. G. Shen, J. R. Sun, Z. H. Cheng, G. H. Rao, and X. X. Zhang, Appl. Phys. Lett. **78**, 3675 (2001).
[3]A. Fujita, S. Fujieda, Y. Hasegawa, and K. Fukamichi, Phys. Rev. B **67**, 104416 (2003).
[4]T. Krenke, E. Duman, M. Acet, E. F. Wassermann, X. Moya, L. Manosa, and A. Plane, Nat. Mater. **4**, 450 (2005).
[5]O. Tegus, E. Brück, K. H. J. Buschow, and F. R. de Boer, Nature **415**, 150 (2002).
[6]E. Liu, W. Wang, L. Feng, W. Zhu, G. Li, J. Chen, H. Zhang, G. Wu, C. Jiang, H. Xu, and F. de Boer, Nat. Commun. **3**, 873 (2012).
[7]V. I. Zverev, A. M. Saletsky, R. R. Gimaev, A. M. Tishin, T. Miyanaga, and J. B. Staunton, Appl. Phys. Lett. **108**, 192405 (2016).
[8]C. F. Sánchez-Valdés, R. R. Gimaev, M. López-Cruz, J. L. Sánchez Llamazares, V. I. Zverev, A. M. Tishin, A. M. G. Carvalho, D. J. M. Aguiar, Y. Mudryk, and V. K. Pecharsky, J. Magn. Magn. Mater. **498**, 166130 (2020).
[9]S. Cervera, M. Trassinelli, M. Marangolo, C. Carrétéro, V. Garcia, S. Hidki, E. Jacquet, E. Lamour, A. Lévy, S. Macé, C. Prigent, J. P. Rozet, S. Steydli, and D. Vernhet, Phys. Rev. Mater. **1**, 065402 (2017).
[10]S. Jacobs, J. Auringer, A. Boeder, J. Chell, L. Komorowski, J. Leonard, S. Russek, and C. Zimma, Int. J. Refrig. **37**, 84–91 (2014).
[11]M. A. Richard, A. M. Rowe, and R. Chahine, J. Appl. Phys. **95**, 2146 (2004).
[12]C. R. H. Bahl, D. Velázquez, K. K. Nielsen, K. Engelbrecht, K. B. Andersen, R. Bulatova, and N. Pryds, Appl. Phys. Lett. **100**, 121905 (2012).
[13]V. B. Chzhan, I. S. Tereshina, A. Y. Karpenkov, and E. A. Tereshina-Chitrova, Acta Mater. **154**, 303 (2018).
[14]J. Liu, T. Gottschall, K. P. Skokov, J. D. Moore, and O. Gutfleisch, Nat. Mater. **11**, 620 (2012).
[15]Y. Y. Gong, D. H. Wang, Q. Q. Cao, E. K. Liu, J. Liu, and Y. W. Du, Adv. Mater. **27**, 801 (2015).
[16]D. H. Mosca, F. Vidal, and V. H. Etgens, Phys. Rev. Lett. **101**, 125503 (2008).
[17]S. K. Giri, P. Dasgupta, A. Poddar, R. C. Sahoo, D. Paladhi, and T. K. Nath, Appl. Phys. Lett. **106**, 023507 (2015).
[18]N. S. Bingham, A. K. Suszka, C. A. F. Vaz, H. Kim, and L. J. Heyderman, Phys. Rev. B **96**, 024419 (2017).
[19]X. Moya, L. E. Hueso, F. Maccherozzi, A. I. Tovstolytkin, D. I. Podyalovskii, C. Ducati, L. C. Phillips, M. Ghidini, O. Hovorka, A. Berger, M. E. Vickers, E. Defay, S. S. Dhesi, and N. D. Mathur, Nat. Mater. **12**, 52 (2013).
[20]Z. B. Guo, Y. W. Du, J. S. Zhu, H. Huang, W. P. Ding, and D. Feng, Phys. Rev. Lett. **78**, 1142 (1997).
[21]P. Chen and Y. W. Du, J. Phys. Soc. Jpn. **70**, 1080 (2001).
[22]R. Venkatesh, M. Pattabiraman, K. Sethupathi, G. Rangarajan, and S. Narayana Jammalamadaka, J. Appl. Phys. **101**, 09C506 (2007).
[23]J. Stankiewicz, J. Sese, J. García, J. Blasco, and C. Rillo, Phys. Rev. B **61**, 11236 (2000).
[24]M. H. Phan, M. B. Morales, N. S. Bingham, H. Srikanth, C. L. Zhang, and S. W. Cheong, Phys. Rev. B **81**, 094413 (2010).
[25]K. Dasa, N. Banub, I. Dasd, and B. N. Devb, J. Magn. Magn. Mater. **487**, 165309 (2019).
[26]R. Kajimoto, H. Yoshizawa, H. Kawano, H. Kuwahara, Y. Tokura, K. Ohoyama, and M. Ohashi, Phys. Rev. B **60**, 9506 (1999).
[27]H. Kuwahara, T. Okuda, Y. Tomioka, A. Asamitsu, and Y. Tokura, Phys. Rev. Lett. **82**, 4316 (1999).
[28]Y. Moritomo, T. Akimoto, A. Nakamura, K. Ohoyama, and M. Ohashi, Phys. Rev. B **58**, 5544 (1998).
[29]Y. Ogimoto, M. Nakamura, N. Takubo, H. Tamaru, M. Izumi, and K. Miyano, Phys. Rev. B **71**, 060403R (2005).
[30]Y. Wakabayashi, D. Bizen, H. Nakao, Y. Murakami, M. Nakamura, Y. Ogimoto, K. Miyano, and H. Sawa, Phys. Rev. Lett. **96**, 017202 (2006).
[31]M. Nakamuraa, Y. Ogimoto, H. Tamaru, M. Izumi, and K. Miyano, Appl. Phys. Lett. **86**, 182504 (2005).
[32]R. A. Cowley, Phys. Rev. **134**, A981 (1964).
[33]A. Okazaki and M. Kawaminami, Mat. Res. Bull. **8**, 545 (1973).
[34]B. M. Zhang, L. J. Wu, W. G. Yin, C. J. Sun, P. Yang, T. Venkatesan, J. S. Chen, Y. M. Zhu, and G. M. Chow, Nano Lett. **16**, 4174 (2016).
[35]K. A. Gschneidner, Jr.,, V. K. Percharsky, A. O. Pecharsky, and C. B. Zimm, Mater. Sci. Forum **315**, 69 (1999).
[36]T. Arima and K. Nakamura, Phys. Rev. B **60**, R15013 (1999).
[37]Y. Herklotz, D. Lee, E. J. Guo, T. L. Meyer, J. R. Petrie, and H. N. Lee, J. Phys.: Condens. Matter. **29**, 493001 (2017).
[38]S. Valencia, A. Gaupp, W. Gudat, A. Balcells, A. Cavallaro, B. Martínez, and F. J. Palomares, Phys. Rev. B **73**, 104402 (2006).